Layer-by-layer assembled fluorescent probes in the second near-infrared window for systemic delivery and detection of ovarian cancer

Xiangnan Dang[a,b,1], Li Gu[a,c,1], Jifa Qi[a,b], Santiago Correa[a,d], Geran Zhang[a,b], Angela M. Belcher[a,b,d,2], and Paula T. Hammond[a,c,2]

[a]Koch Institute for Integrative Cancer Research, Massachusetts Institute of Technology, Cambridge, MA 02139; [b]Department of Materials Science and Engineering, Massachusetts Institute of Technology, Cambridge, MA 02139; [c]Department of Chemical Engineering, Massachusetts Institute of Technology, Cambridge, MA 02139; and [d]Department of Biological Engineering, Massachusetts Institute of Technology, Cambridge, MA 02139

Edited by Michelle Bradbury, Memorial Sloan Kettering, New York, NY, and accepted by the Editorial Board March 14, 2016 (received for review October 27, 2015)

Fluorescence imaging in the second near-infrared window (NIR-II, 1,000–1,700 nm) features deep tissue penetration, reduced tissue scattering, and diminishing tissue autofluorescence. Here, NIR-II fluorescent probes, including down-conversion nanoparticles, quantum dots, single-walled carbon nanotubes, and organic dyes, are constructed into biocompatible nanoparticles using the layer-by-layer (LbL) platform due to its modular and versatile nature. The LbL platform has previously been demonstrated to enable incorporation of diagnostic agents, drugs, and nucleic acids such as siRNA while providing enhanced blood plasma half-life and tumor targeting. This work carries out head-to-head comparisons of currently available NIR-II probes with identical LbL coatings with regard to their biodistribution, pharmacokinetics, and toxicities. Overall, rare-earth-based down-conversion nanoparticles demonstrate optimal biological and optical performance and are evaluated as a diagnostic probe for high-grade serous ovarian cancer, typically diagnosed at late stage. Successful detection of orthotopic ovarian tumors is achieved by in vivo NIR-II imaging and confirmed by ex vivo microscopic imaging. Collectively, these results indicate that LbL-based NIR-II probes can serve as a promising theranostic platform to effectively and noninvasively monitor the progression and treatment of serous ovarian cancer.

second near-infrared window | layer by layer | systemic comparison | ovarian tumor detection | deep penetration

Fluorescence-based optical imaging is a broadly applied imaging technique that provides a nondestructive means for detecting disease, monitoring disease progression, and evaluating treatment outcome (1–4). Compared with tomographic imaging techniques, such as magnetic resonance imaging and computed tomography, fluorescence imaging yields quicker results at a lower cost (5). Fluorescence imaging is categorized according to the spectral regions of the detected signal, including visible (400–750 nm), the first near-infrared window (NIR-I, 750–1,000 nm), and the second near-infrared window (NIR-II; 1,000–1,700 nm). NIR-II fluorescence imaging features deeper penetration and outperforms the others for in vivo investigations owing to the reduced absorption, scattering, and autofluorescence by biological tissues (6, 7).

To clinically translate the benefits of NIR-II imaging, several challenges associated with the delivery of nanoscale NIR-II probes need to be addressed: (*i*) the biocompatibility following systemic administration of NIR-II probes in vivo, (*ii*) a delivery platform that extends the blood circulation time of NIR-II probes to facilitate accumulation in diseased tissues and sustained signal detection, and (*iii*) the successful targeting of NIR-II probes to sites of biomedical interest to provide enhanced diagnostic functionality. Current NIR-II emissive materials, including rare-earth-based down-conversion nanoparticles (DCNPs), quantum dots (QDs), single-walled carbon nanotubes (SWNTs), and small organic molecules, have been incorporated into diagnostic probes using a single lipid, polymer, protein, or bacteriophage (6–12). However, these delivery carriers lack the modularity and versatility to include drugs effectively for theranostic platforms and do not as readily enable the incorporation of complex or multiple drug payloads. Consequently, a modular delivery system of the NIR-II probes is more attractive because it allows incorporation of imaging agents and multiple drugs independently and ability of staged release of therapeutics.

Layer-by-layer (LbL) assembly is a well-established technology that matches the requirements for modularity and versatility to develop theranostic platforms for different NIR-II probes. LbL assembly allows for the construction of hierarchical and multifunctional polyelectrolyte multilayers on a charged colloidal core substrate (13–15), and it is possible to incorporate therapeutics such as siRNA, inhibitors, or proteins in the multilayers around the core nanoparticle (NP) (16). The LbL platform provides improved biocompatibility that reduces off-target toxicity of the delivered payloads (17), and the LbL stealth coatings provide extended blood plasma half-life when applied to liposomes, QDs, gold, and other NP systems (15, 18). Recent work using the LbL platform has led to a demonstration of staged siRNA/chemotherapy

Significance

Survival of cancer patients can be greatly improved by an ideal theranostic platform capable of early detection and effective treatment of tumors. Layer-by-layer (LbL) assembly is a well-established technology and matches the requirement of modularity and versatility for such a theranostic platform. Second near-infrared window (NIR-II) fluorescence imaging is a promising modality with high resolution, deep penetration, and diminished noise. This work, for the first time to our knowledge, establishes a modular and versatile LbL platform for NIR-II agents and presents a head-to-head in vivo comparison of available NIR-II probes. We successfully achieve the selective, noninvasive, and safe detection of high-grade serous ovarian tumors in an orthotopic murine model. These LbL NIR-II probes promise the development of an NIR-II based theranostic platform of disease diagnosis, progression, and treatment.

Author contributions: X.D., L.G., A.M.B., and P.T.H. designed research; X.D., L.G., J.Q., S.C., and G.Z. performed research; X.D. and L.G. contributed new reagents/analytic tools; X.D., L.G., A.M.B., and P.T.H. analyzed data; and X.D., L.G., A.M.B., and P.T.H. wrote the paper.

The authors declare no conflict of interest.

This article is a PNAS Direct Submission. M.B. is a guest editor invited by the Editorial Board.

[1]X.D. and L.G. contributed equally to this work.

[2]To whom correspondence may be addressed. Email: belcher@mit.edu or hammond@mit.edu.

This article contains supporting information online at www.pnas.org/lookup/suppl/doi:10.1073/pnas.1521175113/-/DCSupplemental.

combination release in a triple-negative breast cancer model (13). Furthermore, the LbL system can be used to generate highly effective, dual targeting of outer layers that enables accumulation both through stimuli-responsive behavior triggered by the hypoxic tumor microenvironment and through the binding of ligands overexpressed on tumor cell membranes (14). The considerable control and flexibility of the LbL platform makes it ideal for preparing theranostic nanomedicines, because it can load both therapeutics and diagnostics with high capacity (19, 20) and can coat a broad range of nanomaterials down to 10 nm in size while maintaining uniformity, shape, and structure (18).

Despite current efforts of applying NIR-II probes for bioimaging, some of the essential properties relevant for the clinical translation of these probes are either missing or insufficiently characterized for in vivo biomedical applications. Particularly, SWNTs suffer from poor circulation in either lipid-coated or bacteriophage-bound form (11, 21), the pharmacokinetics of NIR-II emissive QDs and organic dyes are rarely reported (8, 10), and real-time whole-body imaging and pharmacokinetics for DCNPs are not reported (9). Furthermore, each material was studied with different delivery systems and instrumentation, contributing to the observed variations in performance across reports. Therefore, we leverage the LbL platform to generate NIR-II probes with a reproducible and biocompatible targeting stealth coating to facilitate the head-to-head comparison of these materials in vivo.

In this paper, we generate LbL NIR-II NPs with identical polymer multilayer modifications to provide a comprehensive side-by-side evaluation of the available NIR-II materials for in vivo real-time whole-body circulation, pharmacokinetics, biodistribution, toxicities, and applications in disease detection. Different LbL NIR-II NPs broadly exhibit prolonged blood circulation, a critical factor that allows NPs to accumulate in diseased sites. Comparison of these NPs affords clinically relevant information on currently available NIR-II probes and reveals their benefits and drawbacks, providing guidance for potential clinical translation. Overall, LbL-modified DCNPs exhibit excellent signal-to-noise ratio, low toxicity, and long circulation and are selected to demonstrate diagnostic capabilities within ovarian tumor, typically diagnosed at advanced stage. Both in vivo imaging and histology of the diseased tissues suggest preferential accumulation of LbL DCNPs in the tumors, indicating that LbL NIR-II NPs may act as an effective diagnostic platform. Moreover, the modular nature of the LbL platform allows us to further functionalize these materials, particularly through the incorporation of therapeutics to transform the formulations discussed in this work into theranostic NPs.

Results and Discussion

Preparation and Characterization of LbL NIR-II NPs. LbL NPs were constructed for NIR-II probes, including an organic dye (IR1061), SWNT, QD (PbS), and DCNP ($NaY_{0.78}Yb_{0.2}Er_{0.02}F_4$) (Fig. 1 *A* and *B*). Each of the hydrophobic nanoscale NIR-II probes (dye, QD, and DCNP) was first encapsulated in the amphiphilic partially alkyl amide functionalized poly(acrylic acid) (PAA) to yield a net negatively charged core (~100 nm in diameter) for LbL assembly. In the case of the SWNT system, a negatively charged core was first created using sodium cholate stabilized SWNTs to undergo ligand exchange with the modified PAA. Biocompatible poly(L-arginine) (PLA, 10 kDa) and dextran sulfate (DXS, 10 kDa) were the barrier layers. Hyaluronic acid (HA, 40 kDa) for the outmost layer is a natural polysaccharide that extends blood circulation, targets CD44 (a largely expressed receptor in many cancer cell lines), and provides tunable surface chemistry for further modifications. Successful LbL assembly was confirmed by dynamic light scattering (DLS) size measurements that indicated a 10-nm growth following the deposition of each barrier layer and a 40-nm growth following the deposition of terminal HA layer (Fig. 1*C*). Further validation of

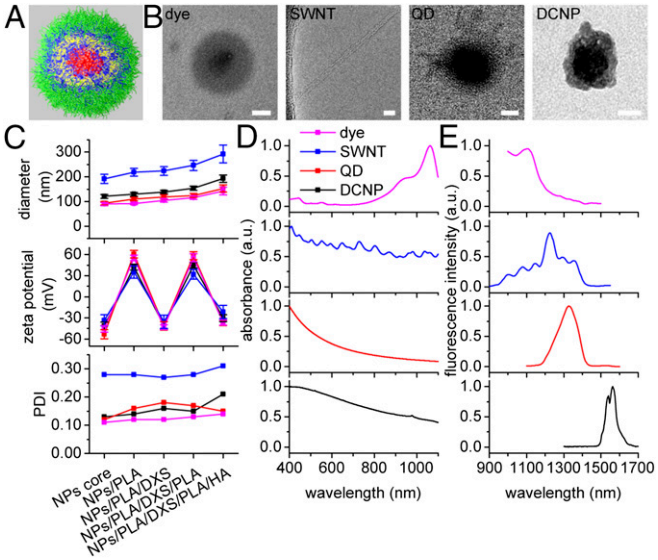

Fig. 1. Characterization of the LbL NIR-II NPs. (*A*) Illustration of a spherical LbL NIR-II NP. From inside to outside: NIR-II core (red), PLA (blue), DXS (yellow), PLA (blue), and HA (green). (*B*) TEM images of the LbL NIR-II NPs. [Scale bars: 50 nm (5 nm for SWNT).] (*C*) DLS characterizations of the NPs for each LbL step, including hydrodynamic diameter, zeta potential, and PDI. Data are given in mean ± SD, $n = 3$. (*D* and *E*) Normalized absorption (*D*) and emission (*E*) spectra of the NPs.

layer deposition was provided by electrophoretic measurements that indicated a complete reversal of surface charge following each layer deposition (Fig. 1*C*). The completed LbL NPs, with a layered structure consisting of NIR-II emissive core/PLA/DXS/PLA/HA, possessed zeta potentials of approximately −30 mV and hydrodynamic diameters within the optimal range (10–200 nm) for systemic delivery (22, 23), except the SWNT (280 nm) because its unique elongated shape was not recognized correctly by DLS measurement. Whereas the polydispersity index (PDI) of dye, QD, and DCNP systems falls between 0.1 and 0.2, indicating monodisperse LbL NPs, the higher PDI of 0.3 for LbL SWNTs was owing to the variation in length of the starting SWNTs (Fig. 1*C*). In addition, transmission electron microscopy (TEM) confirmed the layered structure of LbL NPs (Fig. 1*B*). A thin LbL polyelectrolyte complex coating was observed for each of the three spherical NPs; it should be noted that the LbL films consist of highly interpenetrated carbon-based polyion blends, and thus individual polyelectrolyte layers were indistinguishable in TEM. SWNTs of 3 nm in diameter were observed as singular nanotubes on a holey grid after LbL assembly, indicating that nanotubes presented primarily as individual rather than aggregate structures. It was suggested that the charged SWNTs remained sterically stabilized during LbL assembly, thus retaining efficient fluorescence. Before studying the LbL NIR-II NPs for in vivo imaging, optical absorption and emission spectra were measured (Fig. 1 *D* and *E* and Fig. S1). NIR-II probes were excited with either an 808-nm or a 980-nm laser depending on the unique excitation properties of each probe, while maintaining a large spectral separation between excitation wavelengths and main emission peaks (*SI Results and Discussion* and Fig. S2). The excitation wavelengths and emission peaks (shown as $\lambda_{ex}/\lambda_{em}$ in nanometers) of LbL NPs were 808/1,100 for dye complex, 808/1,225 for SWNT, 980/1,350 for QD, and 980/1,575 for DCNP system (Fig. 1*E*). Under these excitation and emission conditions, the dye complex (3,285 cm^{-1}) and QD (2,797 cm^{-1}) possessed smaller Stokes shift than the SWNT (4,213 cm^{-1}) and DCNP (3,855 cm^{-1}) systems.

Biodistribution and Pharmacokinetics of LbL NIR-II NPs. To evaluate and compare the different LbL-coated NIR-II probes for

biomedical applications, biodistribution and pharmacokinetics studies of each LbL NP type were performed in BALB/c female mice. Whole-body real-time fluorescence imaging was carried out using a custom-built imager, consisting of 808-nm and 980-nm lasers, a silicon camera for bright-field images, and an InGaAs camera taking NIR-II fluorescence images. During whole-body imaging, mice were placed under anesthesia and arranged in either the dorsal or lateral position and injected with LbL NPs via a catheterized tail vein. Immediately following the bolus injections of the NPs, fluorescence images were acquired continuously for 5 min; during this immediate time period, because the NPs were introduced rapidly throughout the bloodstream most organs were clearly recognized (Movie S1, with play speed 10× faster). To study the long-term distributions of the NPs, the whole-body bright-field and fluorescence images were collected at multiple time points ranging from 5 min to 72 h postinjection (Fig. 2*A*). At the same time points, blood samples were drawn and analyzed to assess NP pharmacokinetics (Fig. 2*D*). Additionally, time-dependent biodistribution of LbL NPs was quantified from injection to 72 h postinjection based on the in vivo fluorescence images (Fig. 2*E*), and end-point ex vivo biodistribution was quantified based on the fluorescence images of the harvested organs at 72 h postinjection (Fig. 2*F*).

Several similar features of the biodistribution and pharmacokinetics were observed among the LbL NIR-II NPs. For the biodistribution study, the NPs localized to the heart within 10 s and began to accumulate in the lungs, liver, spleen, and circulatory system at ∼30 s (Movie S1 and Fig. 2*E*). The fluorescence intensities of various major organs remained relatively stable during the remaining part of the video and for up to 1 h. At later time points, fluorescent signals decayed in the major organs for most of the LbL NPs except dye, indicating the clearance of the

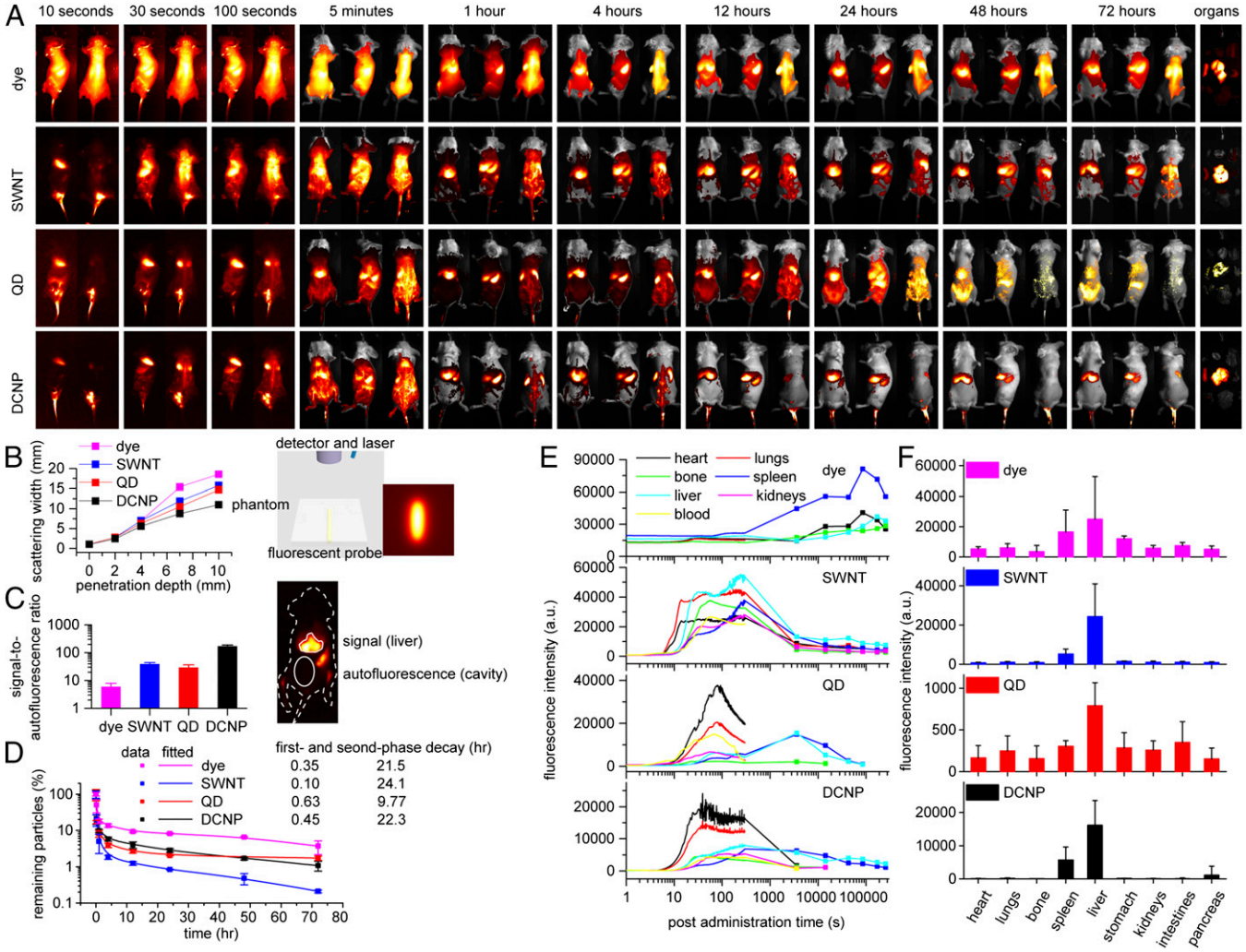

Fig. 2. The biodistribution, pharmacokinetics, and optical properties of LbL NIR-II NPs following i.v. injection in BALB/c mice. (*A*) Whole-body NIR-II images at time points from 10 s to 72 h postinjection. For the first three time points, NIR-II images were extracted from the videos (Movie S1) at lateral (*Left*) and dorsal (*Right*) positions, and for the later time points NIR-II and bright-field images were taken at ventral (*Left*), lateral (*Middle*), and dorsal (*Right*) positions. From left to right and top to bottom, organs were presented in the order of heart, lungs, spine, spleen, liver, stomach, kidneys, intestines, and pancreas. (*B*) The scattering widths of NIR-II signals (*Left*) as a function of the penetration depth through breast-mimic phantoms (*Right*, scheme of the experimental setup and a typical image showing the scattering effect). (*C*) The signal-to-autofluorescence ratios of various NIR-II probes (*Left*) were quantified based on the fluorescence intensities of liver and abdominal cavity (the elliptical area, *Right*); the outline of the mouse is shown as a white dotted line. Data are given as mean + SD, $n = 5$. (*D*) The blood circulation profiles and fitted half-lives using a two-compartment decay model. Data are given as mean ± SD, $n = 3$. (*E*) The dynamic distribution profiles of the LbL NPs in major organs based on the fluorescence intensities from injection time to 72 h postinjection. The intensities up to 5 min (shown as lines) were extracted from the videos, and intensities at later time points (shown as lines and symbols, mean value from three to five measurements) were extracted from the NIR-II images. (*F*) The distribution profiles of NPs in the excised organs based on the fluorescence intensities at 72 h postinjection. Data are given as mean + SD, $n \geq 5$.

NPs prevailed over their accumulation. As expected, the liver and spleen were the main sources of fluorescent signals over the 72-h treatment period (Fig. 2*F*), consistent with the role of these organs in the reticuloendothelial system. Interestingly, NP accumulation was observed in osseous tissues from 30 s to 48 h postinjection, including the spine, femur, and tibia (Fig. 2*A*). Tracking of NPs to osseous tissues demonstrated the benefit of deep penetration gained with NIR-II imaging, because it was difficult to observe with visible and NIR-I imaging.

The pharmacokinetic analysis of the LbL NPs indicated that the probe concentrations in blood experienced a two-phase decay, including the processes of initial rapid distribution and following elimination from tissues. Notably, all LbL NPs, with the exception of the QD system, possessed extended half-lives as long as 24 h (Fig. 2*D*), likely owing to the role of the highly hydrophilic terminal HA layer preventing protein adsorption and opsonization, and the formation of a particularly dense layer in LbL systems achieved upon adsorption to the underlying PLA layer. We have previously examined these PLA/HA systems and found that these extended half-lives were characteristic of weak LbL systems with HA (13, 14, 17). The similarities observed for different NIR-II NPs were likely attributable to the identical LbL surface modifications and demonstrated the efficacy of the LbL platform for facilitating the systemic delivery of diverse material systems. It is noted that the serum stability of the LbL coatings on the surfaces of these very different NIR-II probes is key to achieving the long-term blood circulation required for systemic applications, particularly when examining accumulations that can take place over a period of several days (Fig. S3). The QD system, however, had a half-life of 9 h, much shorter than that of the other systems and different from our observations of LbL QD systems examined in earlier work (15). We believe this difference may be related to the nature of the modified PAA coating on the QD surface, which may not have formed as cohesive an interface with the LbL layers as that achieved with direct layering of a QD synthesized with negatively charged ligands.

Despite the common characteristics among the LbL NIR-II NPs, unique features were observed for each probe. First, for LbL DCNPs at 72 h postinjection, fluorescence intensities were predominantly detected in liver and spleen both in vivo and ex vivo, and the relative intensities from other organs were much lower than those from the other probes, in part due to the long emission wavelength of DCNP, further explained in the next section (Fig. 2*F*). Second, LbL SWNTs exhibited the quickest first-phase decay from blood circulation (0.1 h), followed by a slow second-phase decay (24.1 h) (Fig. 2*D*), in accordance with their rapid initial accumulation and sluggish clearance from the major organs (Fig. 2*E*). For instance, osseous organs including sternum, femur, and spine were identified at as late as 48 h postinjection (Fig. 2*A*), and the relative fluorescence intensities of SWNTs in excised organs were higher than those of DCNPs (Fig. 2*F*). This was attributed to the elongated shape of SWNTs, which may promote tissue penetration and therefore rapidly reduce the concentration of SWNTs in the circulatory system immediately after injection, as well as promote entrapment by the organs to slow excretion from tissues. Third, in contrast to SWNTs, LbL QDs exhibited the slowest first-phase decay (0.63 h) and fastest second-phase decay (9.77 h) (Fig. 2*D*), in agreement with the extended ascending and sudden descending fluorescence profiles of the major organs (Fig. 2*E*). In addition, QDs exhibited the lowest fluorescence intensities in the harvested organs (Fig. 2*F*). Based on previous reports (24, 25), it is thought that QDs (~6 nm), first encapsulated in amphiphilic PAA, can diffuse out of the LbL film and eventually be cleared via the renal system (26, 27). Finally, the LbL dye complex presented an unusual fluorescence profile of the organs, in which the fluorescence intensity peaked at ~24 h postinjection (Fig. 2*E*), suggesting that the dye complex maintained a high concentration in the blood (Fig. 2*D*) and continuously accumulated in the organs for a long time before tissue clearance dominated. It was concluded that, among these LbL NIR-II NPs, DCNPs exhibited the most favorable biodistribution and pharmacokinetics profile, because they offered prolonged first- and second-phase decays, as well as a regular pattern of tissue clearance.

The distinguishing optical properties of various NIR-II probes likely contributed to the observed discrepancies for in vivo and ex vivo fluorescence imaging. In general, probes with longer emission wavelengths can be imaged with higher quality owing to reduced light scattering and tissue autofluorescence. In particular, light scattering decreases monotonically as emission wavelength increases (9, 28, 29). According to their fluorescence emission spectra, we chose optical filter sets of two 1,400-nm long pass + two 1,575-nm band pass, two 1,300-nm long pass + two 1,375-nm band pass, two 1,300-nm long pass, and two 1,100-nm long pass + two 1,125-nm band pass for DCNPs, QDs, SWNTs, and dye complex, respectively, to maximize each probe's signal-to-noise ratio (Table S1). As a result, LbL DCNPs offered NIR-II images with the least scattering and correspondingly defined the vascular and skeletal structures with the highest resolution out of all of the probes (Movie S1 and Fig. 2*A*).

The different scattering of fluorescent signals emitted by NIR-II probes was further investigated using breast-mimic phantoms of various thicknesses. It was observed that the degree of scattering decreased as the emission spectra moved toward longer wavelengths (Fig. 2*B*). The other major source of background noise is autofluorescence, which is known to decrease with larger spectral separation between excitation and emission wavelengths. As mentioned previously, DCNPs and SWNTs process Stokes shift close to or larger than 4,000 cm^{-1}, which is out of the range of the Raman shift of most organic molecules, providing the low level of autofluorescence observed with these probes (30, 31). Instead, QDs and dye complex possess Stokes shift around 3,000 cm^{-1}, strongly overlapping with the Raman shift of organic molecules, resulting in greater autofluorescence, especially in the regions of abdominal cavity and skin (Fig. 2 *A* and *C*). In addition, the excitation wavelength of 808 nm (for dye or SWNTs) resulted in more autofluorescence than the excitation wavelength of 980 nm (for QDs or DCNPs), albeit with similar Raman shift (dye and QDs, or SWNTs and DCNPs), because Raman intensity is inversely proportional to the fourth power of the excitation wavelength (32). The high level of autofluorescence observed for NIR-II imaging with the dye complex likely contributed to the irregular fluorescent signal profiles and low quality of images (Fig. 2 *A* and *E* and Movie S1), as well as the highest fluorescence intensities from excised organs (Fig. 2*F*). Overall, LbL DCNPs offered the optimal optical properties for NIR-II imaging, with the least interference from scattering and autofluorescence, and seemed to be a promising tool for biomedical imaging.

To the best of our knowledge, this is the first report to provide a comprehensive investigation as well as comparison of the biodistribution and pharmacokinetics of the currently available NIR-II fluorescent probes. Further, it is a first look, to our knowledge, at the potential for LbL coatings to address the enhancement of biodistribution for each of four very different NIR-II emissive material systems. All NIR-II probes possessed identical LbL modifications and allowed us to attribute the similarities and differences across these probes to their intrinsic characteristics, morphological or optical. In contrast, the observed variations of performance from different probes among previous reports could be partly owing to extrinsic properties, such as surface charge, surface chemistry, or targeting ligands.

To assess the capabilities of NIR-II imaging to obtain anatomical information, principle component analysis (PCA) was performed to group image pixels with similar time-dependent fluorescence intensities (33). PCA of the video frames of first 5 min postinjection generated composite images that distinguished

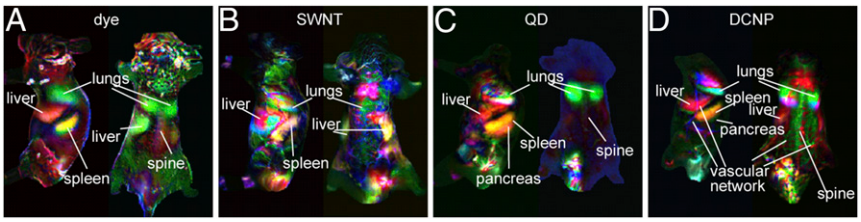

Fig. 3. (*A–D*) PCA of the videos acquired from injection time to 5 min postinjection. For each type of NPs, the lateral (*Left*) and dorsal (*Right*) positions are shown. For each composite image, the red, green, and blue channels represent the combined positive and negative areas of the second, third, and fourth principle components, respectively, from PCA.

various organs with different assigned colors (Fig. 3). For all LbL NIR-II NPs, the main clearance organs (lungs, liver, and spleen) were the major ones identified. Although PCA of SWNTs, QDs, and dye systems showed organ resolution comparable to previous reports (8, 10, 33), video-rate whole-body imaging immediately following i.v. injection of LbL DCNPs and associated PCA is, to our knowledge, first reported in this study. Further, PCA of DCNPs system produced clearer anatomical features, as well as more identified organs, such as pancreas, skin vascular network, and spine, due to the advantages of longer emission wavelength such as deeper penetration, less light scattering, and reduced autofluorescence.

Toxicities of LbL NIR-II NPs. To evaluate the toxicities of the LbL NPs in vivo, the vital organs, including liver, spleen, heart, lungs, and kidneys, were excised and fixed with formalin at 72 h postinjection. Standard H&E staining of the major organs' cross-sections was performed. As examples show in Fig. S4, for tissues from mice treated with all of the probes (*i*) cardiac fibers in the hearts maintained integrity; (*ii*) white pulps, red pulps, and trabecular arteries in the spleens were observed without major damage; and (*iii*) irregular macrophage accumulation in the lungs was not observed in the alveolus space, indicating that LbL NPs did not trigger a severe immune response. In addition, no major damage in the liver or kidneys was observed in mice treated with the dye, SWNTs, and DCNPs systems. However, severe toxicities in liver and kidneys were detected in QDs-treated mice. For instance, focal necrosis and dilated hepatocytes were identified in the liver (circled in Fig. S4*C*), and swollen tubule, a sign of kidney atrophy, was also noted (Fig. S4*C*). Hepato-renal toxicity is a well-known issue preventing the approval of QDs for biomedical applications, and the observed damage is likely attributed to the leakage of the QDs out of the LbL shell (34, 35). To our knowledge, this is the first report of the head-to-head comparison of toxicities of NIR-II probes in an identical LbL platform. In summary, we observed that the LbL-modified dye complex, SWNTs, and DCNPs were functionally nontoxic for biomedical applications. In contrast, these LbL QDs presented severe tissue toxicities; however, past work with LbL QDs suggests that this toxicity is related to leakage of individual QDs from the inner modified PAA encapsulation and LbL films (24, 25, 36).

Detection of Orthotopic Ovarian Tumors Using LbL DCNPs. Owing to their superior biodistribution, pharmacokinetics, and optical properties, LbL DCNPs were used to detect the presence of ovarian tumors in an orthotopic murine model. In this study, COV362 cells were selected based on their genetic similarity to high-grade serous ovarian cancer (HGSOC), the most aggressive ovarian carcinoma subtype (37). The orthotopic tumors were typically formed and disseminated in the cavity after 2 wk following the i.p. implantation of cancer cells into the nude mice. To detect the tumors, the mice received LbL DCNPs as a single i.p. dose. NIR-II fluorescence images of the whole body and excised organs were captured at 72 h postinjection, showing individual disseminated tumor nodules and tumor nodes on normal tissues (Fig. 4*A* and Fig. S5; the bright spots indicate the location of the tumors). Tumors and organs of interest were extracted, fixed with formalin, and stained with H&E. The formation of orthotopic ovarian tumors was confirmed by histopathological features such as irregular cellular shape and crowding, high nuclear-to-cytoplasmic ratio, and a distinct necrotic core (Fig. 4*B*) (7). Furthermore, up-converted visible light by DCNPs (38) allowed us to determine the colocalization of DCNPs and tumorous tissue on the cellular level using two-photon confocal microscopy. The DCNPs were found predominantly in the tumor nodes (Fig. 4*B*), which preferentially uptook LbL DCNPs relative to normal tissues such as the pancreas and intestine (Fig. 4 *C* and *D*). The selectivity is likely due to the HA terminal layer, which binds to the CD44 receptor overexpressed by the COV362 cell line. Notably, in certain instances tumor cell crowding was observed inside the liver, indicative of tumor invasion, where relatively fewer DCNPs were detected in the tumor area (Fig. 4*E*). To our knowledge, this approach to determine colocalization of NPs and tumorous tissue on the cellular level using any other NIR-II probes has not been reported, because most intravital confocal microscopes are not equipped with necessary NIR-II detectors. Instead, DCNPs offer up-converted visible emission for cellular-level detection with low autofluorescence and down-converted NIR-II emission for in vivo imaging with deep penetration. Herein, we provide the first

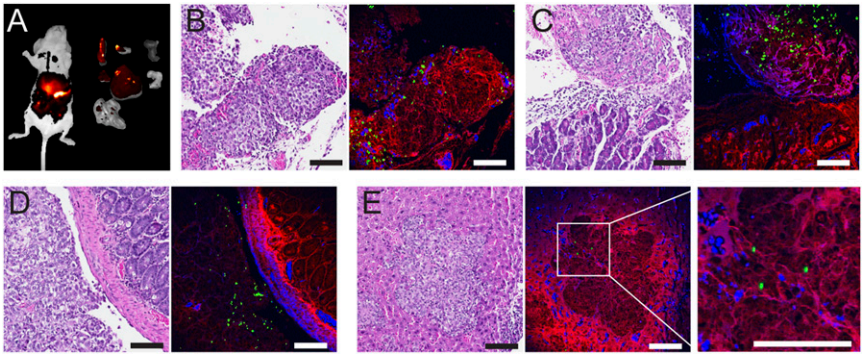

Fig. 4. Targeted detection of orthotopic ovarian tumors. (*A*) NIR-II images of the whole mouse (left) and the excised organs (from left to right and top to bottom are, spleen, ovaries, kidneys, pancreas, liver, stomach, and intestines). The bright spots indicate tumor nodules. (*B–E*) Slices of tumor (*B*), tumor nodules on pancreas (*C*), intestine (*D*), and the tumor invaded the liver (*E*). Each pair show an H&E-stained slice of tissue (*Left*) and the registered multiphoton confocal microscopy (*Right*) where signals from DCNPs (green), hematoxylin (blue), and eosin (red) were composited. (Scale bars: 100 μm.)

proof-of-concept study, to our knowledge, using LbL DCNPs for cancer detection in an HGSOC model and demonstrate the effectiveness and versatility of these modular systems for promising translational applications, from bioimaging to theranostics.

Conclusion. In summary, we constructed LbL-modified NIR-II NPs from currently available NIR-II fluorescent materials to perform a side-by-side investigation and comparison for the biodistribution, pharmacokinetics, and toxicities of these probes. Despite prior research efforts, many benefits and drawbacks among current NIR-II probes remained unexplored. For the first time to our knowledge, these NIR-II probes were directly compared to determine clinically relevant information using the same delivery platform and imaging instrumentation, eliminating previously observed discrepancies generated by such external factors. As a consequence, the findings and achievements in this study are of great interest for research endeavors in NIR-II imaging and provide guidance when applying NIR-II fluorescent probes for biomedical applications.

After weighing both the optical and the pharmacokinetic characteristics of these NIR-II probes, LbL-modified DCNPs provided superior imaging performance and were evaluated as a diagnostic tool in an orthotopic model of HGSOC. The ovarian tumors, either distributed within the abdominal cavity or associated with vital organs such as liver, pancreas, intestine, and so on, were successfully detected in a noninvasive manner. This study concludes that LbL NIR-II NPs can serve as an imaging tool to monitor tumor dissemination, invasion, metastasis, and treatment response, as well as real-time imaging-guided surgery.

Materials and Methods

All materials are provided in *SI Materials and Methods*. Experimental procedures are provided in *SI Materials and Methods*, including synthesis of DCNPs and SWNTs, fabrication and characterization of LbL NIR-II NPs, mouse handling and injection, whole-body imaging, pharmacokinetics, toxicity, cell culture, and tumor induction procedures, calculation of scattering width and signal-to-autofluorescence ratio, PCA, and multiphoton confocal microscopy.

All in vivo experiments were performed under the supervision of the Division of Comparative Medicine, Massachusetts Institute of Technology, and in compliance with the principles of laboratory animal care of the National Institutes of Health.

ACKNOWLEDGMENTS. We thank Abigail Powell for assistance with tail vain injections; Dr. Rod Bronson for assistance with pathological analysis; Dr. Jeffery Wycoff for assistance with two-photon confocal microscopy; Dr. Yong Zhang for assistance with transmission EM; the Koch Institute for Integrative Cancer Research at MIT for providing facilities to support this work; Department of Comparative Medicine at the Massachusetts Institute of Technology; the Koch Institute Swanson Biotechnology Center for assistance with animal experiments; and the Koch Institute Frontier Research Program through the Kathy and Curt Marble Cancer Research Fund. This work was supported by Department of Defense Ovarian Cancer Research Program TEAL Innovator Award OC120504 (to P.T.H) and National Cancer Institute Center for Cancer Nanotechnology Excellence Grant 5-U54-CA151884-03 (to A.M.B.). This material is based upon work supported by National Science Foundation Graduate Research Fellowship Grant 1122374 (to S.C.).

1. Jung HK, Wang K, Jung MK, Kim IS, Lee BH (2014) In vivo near-infrared fluorescence imaging of apoptosis using histone H1-targeting peptide probe after anti-cancer treatment with cisplatin and cetuximab for early decision on tumor response. *PLoS One* 9(6):e100341.
2. van Dam GM, et al. (2011) Intraoperative tumor-specific fluorescence imaging in ovarian cancer by folate receptor-α targeting: First in-human results. *Nat Med* 17(10):1315–1319.
3. Zhang X, et al. (2015) Near-infrared fluorescence molecular imaging of amyloid beta species and monitoring therapy in animal models of Alzheimer's disease. *Proc Natl Acad Sci USA* 112(31):9734–9739.
4. Zhu A, et al. (2015) Dually pH/reduction-responsive vesicles for ultrahigh-contrast fluorescence imaging and thermo-chemotherapy-synergized tumor ablation. *ACS Nano* 9(8):7874–7885.
5. Weissleder R, Pittet MJ (2008) Imaging in the era of molecular oncology. *Nature* 452(7187):580–589.
6. Hong G, et al. (2012) Multifunctional in vivo vascular imaging using near-infrared II fluorescence. *Nat Med* 18(12):1841–1846.
7. Ghosh D, et al. (2014) Deep, noninvasive imaging and surgical guidance of submillimeter tumors using targeted M13-stabilized single-walled carbon nanotubes. *Proc Natl Acad Sci USA* 111(38):13948–13953.
8. Hong G, et al. (2012) In vivo fluorescence imaging with Ag2S quantum dots in the second near-infrared region. *Angew Chem Int Ed Engl* 51(39):9818–9821.
9. Naczynski DJ, et al. (2013) Rare-earth-doped biological composites as in vivo shortwave infrared reporters. *Nat Commun* 4:2199.
10. Tao Z, et al. (2013) Biological imaging using nanoparticles of small organic molecules with fluorescence emission at wavelengths longer than 1000 nm. *Angew Chem Int Ed Engl* 52(49):13002–13006.
11. Yi H, et al. (2012) M13 phage-functionalized single-walled carbon nanotubes as nanoprobes for second near-infrared window fluorescence imaging of targeted tumors. *Nano Lett* 12(3):1176–1183.
12. Diao S, et al. (2015) Fluorescence imaging in vivo at wavelengths beyond 1500 nm. *Angew Chem Int Ed Engl* 54(49):14758–14762.
13. Deng ZJ, et al. (2013) Layer-by-layer nanoparticles for systemic codelivery of an anticancer drug and siRNA for potential triple-negative breast cancer treatment. *ACS Nano* 7(11):9571–9584.
14. Dreaden EC, et al. (2014) Bimodal tumor-targeting from microenvironment responsive hyaluronan layer-by-layer (LbL) nanoparticles. *ACS Nano* 8(8):8374–8382.
15. Poon Z, Lee JB, Morton SW, Hammond PT (2011) Controlling in vivo stability and biodistribution in electrostatically assembled nanoparticles for systemic delivery. *Nano Lett* 11(5):2096–2103.
16. Elbakry A, et al. (2009) Layer-by-layer assembled gold nanoparticles for siRNA delivery. *Nano Lett* 9(5):2059–2064.
17. Dreaden EC, et al. (2015) Tumor-targeted synergistic blockade of MAPK and PI3K from a layer-by-layer nanoparticle. *Clin Cancer Res* 21(19):4410–4419.
18. Schneider G, Decher G (2004) From functional core/shell nanoparticles prepared via layer-by-layer deposition to empty nanospheres. *Nano Lett* 4(10):1833–1839.
19. Ai H (2011) Layer-by-layer capsules for magnetic resonance imaging and drug delivery. *Adv Drug Deliv Rev* 63(9):772–788.
20. Soike T, et al. (2010) Engineering a material surface for drug delivery and imaging using layer-by-layer assembly of functionalized nanoparticles. *Adv Mater* 22(12):1392–1397.
21. Liu Z, et al. (2008) Circulation and long-term fate of functionalized, biocompatible single-walled carbon nanotubes in mice probed by Raman spectroscopy. *Proc Natl Acad Sci USA* 105(5):1410–1415.
22. Blanco E, Shen H, Ferrari M (2015) Principles of nanoparticle design for overcoming biological barriers to drug delivery. *Nat Biotechnol* 33(9):941–951.
23. Alexis F, Pridgen E, Molnar LK, Farokhzad OC (2008) Factors affecting the clearance and biodistribution of polymeric nanoparticles. *Mol Pharm* 5(4):505–515.
24. Hu R, et al. (2012) PEGylated phospholipid micelle-encapsulated near-infrared PbS quantum dots for in vitro and in vivo bioimaging. *Theranostics* 2(7):723–733.
25. Cao J, et al. (2012) In vivo NIR imaging with PbS quantum dots entrapped in biodegradable micelles. *J Biomed Mater Res A* 100(4):958–968.
26. Choi HS, et al. (2007) Renal clearance of quantum dots. *Nat Biotechnol* 25(10):1165–1170.
27. Antaris AL, et al. (2016) A small-molecule dye for NIR-II imaging. *Nat Mater* 15(2):235–242.
28. Balu M, et al. (2009) Effect of excitation wavelength on penetration depth in nonlinear optical microscopy of turbid media. *J Biomed Opt* 14(1):010508.
29. van Leeuwen-van Zaane F, et al. (2013) In vivo quantification of the scattering properties of tissue using multi-diameter single fiber reflectance spectroscopy. *Biomed Opt Express* 4(5):696–708.
30. Diao S, et al. (2015) Biological imaging without autofluorescence in the second near-infrared region. *Nano Res* 8(9):3027–3034.
31. del Rosal B, Villa I, Jaque D, Sanz-Rodríguez F (2015) In vivo autofluorescence in the biological windows: The role of pigmentation. *J Biophotonics*, 10.1002/jbio.201500271.
32. McCreery RL (2005) *Raman Spectroscopy for Chemical Analysis* (Wiley, New York).
33. Welsher K, Sherlock SP, Dai H (2011) Deep-tissue anatomical imaging of mice using carbon nanotube fluorophores in the second near-infrared window. *Proc Natl Acad Sci USA* 108(22):8943–8948.
34. Su Y, et al. (2011) In vivo distribution, pharmacokinetics, and toxicity of aqueous synthesized cadmium-containing quantum dots. *Biomaterials* 32(25):5855–5862.
35. Valizadeh A, et al. (2012) Quantum dots: Synthesis, bioapplications, and toxicity. *Nanoscale Res Lett* 7(1):480.
36. Tsoi KM, Dai Q, Alman BA, Chan WC (2013) Are quantum dots toxic? Exploring the discrepancy between cell culture and animal studies. *Acc Chem Res* 46(3):662–671.
37. Domcke S, Sinha R, Levine DA, Sander C, Schultz N (2013) Evaluating cell lines as tumour models by comparison of genomic profiles. *Nat Commun* 4:2126.
38. Wang M, et al. (2009) Immunolabeling and NIR-excited fluorescent imaging of HeLa cells by using NaYF(4):Yb,Er upconversion nanoparticles. *ACS Nano* 3(6):1580–1586.
39. Ye X, et al. (2010) Morphologically controlled synthesis of colloidal upconversion nanophosphors and their shape-directed self-assembly. *Proc Natl Acad Sci USA* 107(52):22430–22435.
40. Somers RC, Snee PT, Bawendi MG, Nocera DG (2012) Energy transfer of CdSe/ZnS nanocrystals encapsulated with rhodamine-dye functionalized poly(acrylic acid). *J Photochem Photobiol Chem* 248:24–29.
41. Liu Z, et al. (2007) In vivo biodistribution and highly efficient tumour targeting of carbon nanotubes in mice. *Nat Nanotechnol* 2(1):47–52.
42. Hong G, et al. (2014) Ultrafast fluorescence imaging in vivo with conjugated polymer fluorophores in the second near-infrared window. *Nat Commun* 5:4206.
43. Welsher K, et al. (2009) A route to brightly fluorescent carbon nanotubes for near-infrared imaging in mice. *Nat Nanotechnol* 4(11):773–780.